



# Quantitative investigation of the cycling behavior and SEI formation of tin through time-resolved microgravimetry

Ke Wang<sup>a,\*</sup>, Yug Joshi<sup>a,b</sup>, Hong Chen<sup>a</sup>, Guido Schmitz<sup>a</sup>

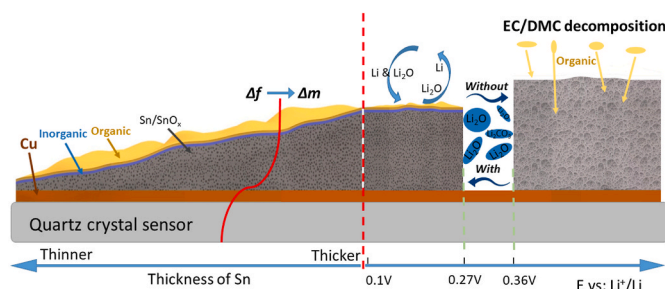
<sup>a</sup> University of Stuttgart, Institute for Materials Science, Chair of Materials Physics, Heisenbergstr. 3, 70569, Stuttgart, Germany

<sup>b</sup> Karlsruhe Institute of Technology, Institute for Applied Materials - Energy Storage Systems, Hermann-von-Helmholtz-Platz 1, 76344, Eggenstein-Leopoldshafen, Germany

## HIGHLIGHTS

- The SEI formation on Sn is investigated by combined QCM and CV.
- The linear relation between electrode thickness and SEI thickness.
- The proportion of oxidized tin increase with Sn thickness increase.
- The inorganic SEI is important for stabilizing the electrode against corrosion.

## GRAPHICAL ABSTRACT



## ARTICLE INFO

### Keywords:

Tin battery anode  
In-situ quartz crystal microbalance  
Solid electrolyte interface  
Cycling behavior

## ABSTRACT

Insufficient understanding on the mechanism of electrode failure restricts the development of sensitive electrode materials such as tin-based alloys. Here-in, a non-destructive and time-resolved in-situ characterization method is proposed for the investigation of the electrode failure. The cycling behavior of tin electrode and the evolution of the Solid-Electrolyte Interface (SEI) were investigated via combining quartz crystal micro-gravimetry (QCM) with cyclic voltammetry (CV). Key findings were further confirmed by ex-situ SEM, TEM and XPS. Remarkably, opposite to the general behavior, SEI thickness grows linearly with the electrode's thickness. This is ascribed to the continuous cracking and oxidization of Sn. However, below a critical thickness ( $X_{sn}$ ), the SEI growth by cracking ( $X_{sn} > X_c$ ) transitions to diffusion-controlled growth ( $X_{sn} \leq X_c$ ). Surprisingly, after serious fracture of Sn, the QCM mass spectrometry reveals, the mass of  $\text{Li}_2\text{O}$  also cycled reversibly along with Li insertion. Despite the general belief that the SEI is formed before the lithiation, the inorganic SEI mainly composed of  $\text{Li}_2\text{O}$  and  $\text{Li}_2\text{CO}_3$  unexpectedly forms in the later cycles during the lithiation. This inorganic part of the SEI plays the most important role of stabilizing the SEI. Preventing its formation, by using an unsuitable voltage window, results in a completely porous non-self-limiting SEI along with a porous electrode.

\* Corresponding author.

E-mail address: [Ke.Wang@mp.imw.uni-stuttgart.de](mailto:Ke.Wang@mp.imw.uni-stuttgart.de) (K. Wang).

## 1. Introduction

Rechargeable lithium-ion batteries (LIBs) are essential for present-day devices in transportable or mobile application. Although, LIBs bring already great convenience, the needs for higher specific capacity, longer lifetime and safety, especially in electric vehicles, cannot be disputed [1–3]. In this regard, tin (Sn) is considered as one of the promising anode materials for high capacity ( $994 \text{ mAh g}^{-1}$ ) which is 2.67 times of that of graphite ( $372 \text{ mAh g}^{-1}$ ) [4–6]. However, a 257% volume expansion caused by formation of the  $\text{Li}_{14}\text{Sn}$  intermetallic phase, and the re-crystallization of Sn leads to pronounced stress and fracture of Sn. Thereby, Sn and Sn-based anodes are seriously limited in long-term stability [7].

Apart from the lithiation and de-lithiation of the electrode, there are interfacial side reactions occurring, such as the decomposition of the electrolyte and the formation of a solid electrolyte interphase (SEI) [8] [–] [11]. Generally, the formation/existence of an SEI is a double-edged sword. On the one hand, the formation of SEI consumes lithium and also increases the resistance against further lithium insertion, which cause an irreversible fade of capacity and rate capability. On the other hand, SEI serves as a protecting layer which prevents the electrode from the continuous corrosion in contact to the electrolyte and thus stabilizes the electrode [12]. Due to the crucial role of the SEI, recent research increasingly investigates how the SEI affects the LIB capacity, lifetime, and safety [13–16]. Different to other anodes, such as graphite, Si or Ge, tin grains tend to coarsen at room temperature, because of the extremely low recrystallization temperature of (224 K) [17]. This causes the electrode and the SEI continuously cracking and re-forming even during the delithiation [18]. Thus, it is necessary to have a clear understanding of the formation of SEI on tin, which can serve as a guide to further optimize these electrodes.

Roughly, the methods of SEI characterization may be divided into two categories: in-situ and ex-situ methods. Ex-situ methods can use advanced instruments to precisely characterize the composition and morphology of SEI. However, because of the sensitivity of SEI, the inevitable exposure to air during sample transfer or artefacts of sample preparation can lead to misleading results. Besides, ex-situ techniques only provide a few snapshots of certain stages of the battery operation, whereas, SEI formation is a continuous process. Thus, an in-situ characterization method is attractive for further study of this process. Some instances exist in the literature. In-situ atomic force microscopy was used to study surface microstructure of a Sn electrode by Beaulieu et al. who found the pulverization of Sn caused by inhomogeneous volume expansion leads to the continuous consumption of electrode and electrolyte [13]. Kyong et al. used in-situ TEM to study morphological changes in and around Sn electrodes. They found insignificant morphological changes during lithiation, but formation of nanoscale porosity and surface roughness during de-lithiation [19]. These available in-situ studies were focused on the characterization of the microstructure, while significant quantitative data on the evolution of SEI and its composition are not available.

Recently, quartz crystal microbalance (QCM) has gained attention in the characterization of SEI formation [20–22], as it can detect the in-situ mass change during the lithiation and delithiation. The loaded mass is determined by the change in resonance frequency of the quartz crystal upon loading/unloading according to the well-known Sauerbrey equation [23] (see section experiment). The sensitive detection of the frequency change allows a precise measurement of mass changes within the range of nanograms [21,24,25]. QCM can be combined with electro-chemical characterization especially Cyclic Voltammetry (CV). To deduce the composition of SEI, Terwort et al. proposed a detailed, time resolved in-situ mass spectrometry based on QCM that even enables in suitable cases the identification of reversibly or irreversibly processed species (at the example of  $\text{V}_2\text{O}_5$ ) [26]. With this technique, later the long-term cycling behavior of Si was studied by Kohler et al. [27] Remarkably, they found that half of the chemical storage of thin film Si

electrodes is not due to lithiation but due to reversible adsorption of  $\text{Li}_2\text{O}$  to the SEI layer [27].

In our previous work [28], the complex SEI formation process in case of 100 nm Sn films was presented and a four-stage sequence of SEI formation was discovered: Stage I comprises only the first charging-/discharging cycle. A layer of organic and inorganic SEI formed even before significant lithiation. Stage II sets in with the second cycle. Further growth of inorganic SEI ( $\text{Li}_2\text{O}$  and more complex oxides) is detected during the lithiation half cycle in the potential range of 0.36–0.27 V. In addition, Sn begins to become oxidized in the delithiation half cycles (above 0.92 V). The 6th cycle marks the onset of stage III, in which the deposition of irreversible  $\text{Li}_2\text{O}$  stops and further significant growth of the SEI is noticed only by the oxidation of Sn during the delithiation. Transition to the final stage IV is observed at about the 45th cycle. This stage is distinguished by an almost stable SEI, that only grows slowly probably under diffusion control. As the second interesting aspects discovered by quantitative analysis of the processed mass, a heavier species (probably  $\text{Li}_2\text{O}$ ) is demonstrated to contribute with a relative fraction of 23% to the reversible charge storage with 100 nm thick Sn films.

The goal of the present work is a further clarification of the mechanisms of the SEI formation on Sn anodes by means of controlled variation of the electrode thickness and of the potential window of operation. Samples used in this work were deposited by physical vapor deposition (ion-beam sputtering) which conveniently enables the quantitative control of different thicknesses. In addition, sputter deposited films have the advantage of being free from conductivity or binder additives excluding the interference with these factors.

Although, SEI formation is presumed to be a surface effect, we find that the thickness of Sn electrode has an unexpected clear impact on the SEI growth. A linear relation is found between the electrode thickness and the SEI thickness, which we link to continuous cracking and oxidation of Sn. Remarkably, the mass of  $\text{Li}_2\text{O}$  is cycled as a reversible species of which the relative amount increases with Sn thickness. Furthermore, we can demonstrate that especially the formation of inorganic SEI, mainly consisting of  $\text{Li}_2\text{O}$  and  $\text{Li}_2\text{CO}_3$ , during the stage II is of utmost importance for the protection capability of SEI. If this process is hindered by unsuitable electrode thicknesses or voltage windows, the electrode continuously cracks and even becomes a fully porous layer.

## 2. Experiment and data analysis

### 2.1. Thin film deposition

Ion beam sputtering was used to prepare tin and copper (Cu) thin films within a custom-made ultrahigh vacuum ( $1 \times 10^{-7}$  mbar) chamber equipped with an Ion-Tech KF/F 40 Kaufman-type ion-source. During the sputtering, 2.0 sccm Argon (99.999% Ar) was used as process gas at a working pressure of about  $10^{-3}$  mbar. A beam voltage of 1 kV, a beam current of 21 mA and an acceleration voltage of 100 V resulted in a moderately fast growth rate ( $0.9 \text{ \AA/s}$  for Cu and  $1.1 \text{ \AA/s}$  for Sn). As substrates, gold-coated 5 MHz quartz QCM sensors (delivered from Renlux crystal) were used, on which first a layer of 100 nm Cu (current collector) was deposited followed by Sn anodes of 20 nm, 50 nm, 100 nm or 150 nm. A sketch of the sample geometry is shown in Fig. 1(a). During growth, the thickness of the growing films was measured with a quartz crystal thickness monitor (SQM-160, Inficon) placed next to the substrate. The final thickness of the deposited films was confirmed by transmission electron microscopy (TEM).

### 2.2. In-situ mass change measurement during charging and discharging

In-situ mass change has been measured during lithiation and delithiation of the Sn electrode using a quartz crystal microbalance (Maxtex RQCM). Simultaneously, the control of the working-potential during Cyclic Voltammetry (CV) was performed using a BioLogic VSP-300. A

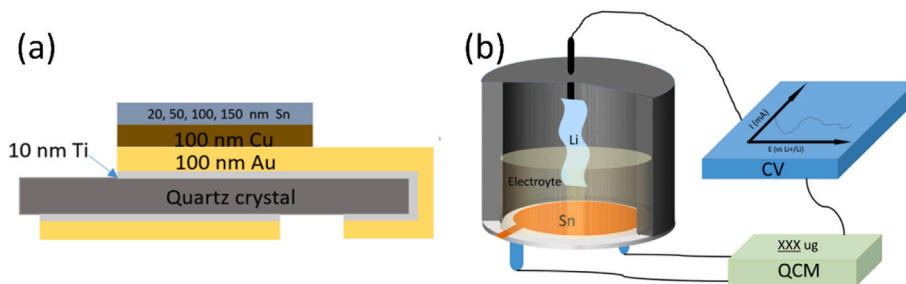


Fig. 1. Scheme of (a) the working electrode and (b) the setup for the CV-QCM measurement.

sketch of the experimental setup is shown in Fig. 1(b).

A custom-made cell was used to cycle at a rate of 0.5 mV/s in different potential windows. To prevent the detrimental effects of oxygen and humidity, both assembly and cycling were performed inside a glovebox ( $O_2$  and  $H_2O$  content <0.5 ppm). A Lithium foil was used as counter and reference electrode, while a mixture of 50 wt% ethylene carbonate (EC, alpha Aesar, 99%), 50 wt% dimethyl carbonate (DMC, sigma Aldrich, 99%), containing 1 mol  $L^{-1}$  lithium perchlorate ( $LiClO_4$ , sigma Aldrich, 99.99%) served as electrolyte. To stabilize the signals, always a 24h OCV measurement was carried out before cycling.

### 2.3. Structural, microstructural and chemical characterization

For a-posteriori characterization, the electrodes were cleaned with DMC to remove residual electrolyte. The surface of the electrode was investigated by Scanning Electron Microscopy (SEM) at 5 kV and 1.6 nA. TEM was used to study the microstructure of the tin electrode and to calibrate its thickness in cross section micrographs obtained with a Philips CM200-FEG microscope operated at 200 kV. A dual beam microscope (Thermo Fischer SCIOS) equipped with a Focused ion beam (FIB) and an e-beam was used to prepare electron transparent lamella via 'lift-out technique' [24]. The crystal structure was characterized by XRD using a Rigaku smartlab 3 kW diffractometer with  $Cu-K\alpha$  radiation, at a scan rate of  $1^\circ/\text{min}$  in the angular range from  $10^\circ$  to  $80^\circ$ . An air tight cell was used that prevented surface contamination and reaction during the XRD test. Therefore, weak signals from the cell window material are included in the XRD pattern. XPS was conducted with a spectrometer from Thermo Fischer Scientific Inc., equipped with an  $Al K\alpha$  X-ray source emitting radiation with an energy of 1486.4 eV.

### 2.4. Data analysis

#### 2.4.1. Capacity

As shown in equation (1), charge (Q) is the integrated current over time, and the volumetric specific capacity was calculated by normalizing the charge to the corresponding volume. For the latter, the surface area of electrode was measured by an optical microscope, while the thickness was measured by using a TEM.

$$C = \frac{Q}{V} = \frac{1}{V} \int I dt \quad (1)$$

#### 2.4.2. Mass from QCM and CV

The mass change from QCM ( $\Delta m_Q$ ) during the lithiation and delithiation cycles was calculated from the change of resonance frequency of the electrode-coated QCM sensor according to the Sauerbrey equation [23].

$$\Delta m_Q = -\frac{\sqrt{\rho \cdot u}}{2n \cdot f^2} \Delta f = -\Delta f \cdot C_f^{-1} \quad (2)$$

Here,  $\rho$  ( $2.65 \text{ g/cm}^3$ ) is the density of the quartz,  $u$  represents the shear modulus of the quartz,  $n$  is the overtone order (here, it is 1) and  $f$  is the resonance frequency of the quartz (in Hz),  $\Delta f$  is the frequency change in

Hz. All the geometric and material-dependent parameters are comprised in the so-called sensitivity factor  $C_f$ , which mainly depends on the thickness of a given quartz crystal. In this work, a 5 MHz Quartz crystal of  $330 \mu\text{m}$  thickness with the corresponding sensitivity factor of  $C_f = 1.767 \cdot 10^{-8} \text{ Hz ng}^{-1} \text{ cm}^{-2}$  has been used. The sensitivity factor was calibrated based on the electrodeposition of a Cu film. The detection limit of the QCM controller (Maxtek RQCM) is 0.1 Hz, which corresponds to a mass change sensitivity of  $1.8 \text{ ng cm}^{-2}$ .

The mass change from CV ( $\Delta m_{CV}$ )

$$\Delta m_{CV} = m_{Li} \cdot \frac{Q}{e} \quad (3)$$

Where  $m_{Li}$  ( $1.15258 \cdot 10^{-23}$ ) is the mass of one lithium atom,  $Q$  is the measured charge and  $e$  ( $1.602 \cdot 10^{-19} \text{ C}$ ) is the elementary charge. This mass change assumes only lithium ions are transferred to or desorbed from the electrode. In view of the fact that other reversible species may be processed reversibly too,  $m_{corrected}$  is partly used instead of  $m_{Li}$ , where the value of  $m_{corrected}$  represents an average that depends on the types and proportions of other reversible species.

$$\Delta m_{CV,corrected} = m_{corrected} \cdot \frac{Q}{e} \quad (4)$$

#### 2.4.3. Mass per charge

In order to quantify the amount of specific species inserted during an electrochemical reaction, QCM mass and CV charge data are combined to get the real time Mass Per Elementary charge (MPE) (equation (5)), which could be used to conclude for the main species processed during the considered cycling period.

$$\text{MPE} = \frac{-e \cdot \Delta m}{I \Delta t} \quad (5)$$

#### 2.4.4. Time-resolved mass spectra

In order to intuitively observe the amount of each processed species, mass spectra are derived based on many MPE values. To this aim, the MPE values were calculated with equation (5) for many time intervals (13 s) and then assorted into a histogram with a class width of  $1 \text{ g mol}^{-1}$ . In the histograms plotted in the following, a negative mass on the x axis indicates delithiation (decrease of mass), and a positive mass represents lithiation (increase of mass).

## 3. Results and discussion

Sn electrodes in different thickness were deposited by ion-beam sputtering (see experiment section). Fig. 2 (a) – (d) respectively present the SEM surface images of Sn films of different thickness (20 nm, 50 nm, 100 nm and 150 nm) deposited by ion-beam sputtering. The microstructures of the as-prepared films show a pronounced but similar surface roughness independent of thickness. Significant roughness of Sn films has been reported in previous work and is attributed to the very low melting temperature of Sn ( $T_m = 231.9^\circ \text{C}$ ) [17] and thus relatively low surface energy. To measure the mass change during the charging

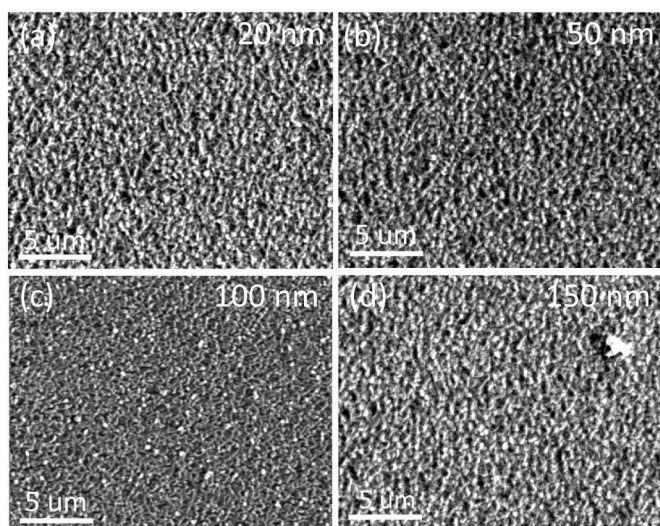


Fig. 2. SEM surface images of different thickness of Sn (a) 20 nm, (b) 50 nm, (c) 100 nm and (d) 150 nm.

and discharging, different thicknesses of Sn deposited on the QCM sensor were cycled in a custom-made set up (see experiment section).

### 3.1. Electrochemical performance of Sn anodes of different thickness

Fig. 3 shows the CV curves of Sn electrodes of different thicknesses (20 nm, 50 nm, 100 nm and 150 nm) cycled at a scan rate of 0.5 mV/s in a potential window of 0.1–1.5 V (with respect to Li reference). Based on our previous work on the SEI formation on Sn [28], the 1st, 2nd, 20th and 80th cycles can well reflect the four main stages of SEI formation. As seen in Fig. 3 (b)–(d), the CV curves of 50 nm, 100 nm and 150 nm Sn anodes show a similar electrochemical cycling behavior. In the first cycle (black), the negative current peak at 0.6 V represents the

formation of inorganic SEI, while the negative peak at 0.15 V and the positive peaks at 0.7 V, 0.78 V, 0.86 V correspond to the lithiation and delithiation, respectively [29]. Also shifts and weakening of the peaks with increasing cycle number are very similar for these thicknesses. By contrast, as shown in Figs. 3 (a), 20 nm Sn exhibits a significantly different redox behavior in the 1st (black) and 2nd cycle (red). In detail, the negative current peak at around 0.6 V is weaker, indicating only negligible formation of inorganic SEI for this thickness. Instead a shoulder at 0.4 V indicates a peak that is observed in the thicker films only in the later cycles. In addition, the characteristic triplet of positive peaks observed during de-intercalation of thick films from 0.7 to 0.9 V is not seen. It appears that the transition into the stages II and III appears way faster for the thinnest film (indeed, after only one cycle). On the other hand, the CV of the late 20th and 80th cycles (representing stage III and IV) are quite similar for all four layer thicknesses.

So, the SEI formation and cycling behavior of 20 nm thick Sn must be studied separately and this should be focused to stages I and II. Based on the CV data, the electrochemical capacity of the different Sn anodes was calculated by integrating current over time (equation (1) in experiment section). The capacities of all samples decrease continuously with cycle number until around the 60th cycle and then remain at around 600–750 mAh cm<sup>-3</sup> (see Fig. S1 in the supplementary material). This capacity fade has been discussed in our previous work [28].

### 3.2. The dependence of SEI growth on the Sn thickness

In order to investigate the effect of sample thickness on the formation of SEI, the mass changes of four different sample thicknesses (20 nm, 50 nm, 100 nm, and 150 nm) as measured by QCM are shown in Fig. 4 (a). As already discussed in previous work [28], the characteristic periodic oscillations represent the reversible process of lithiation and delithiation, while the continuous increase of the averaged baselines indicates an irreversible mass deposition (mostly attributed to the SEI formation). Qualitatively, the mass changes of the four samples demonstrate a very similar trend. With progress of cycling, the oscillation amplitude decreases, which reflects the capacity fade. But more important in this

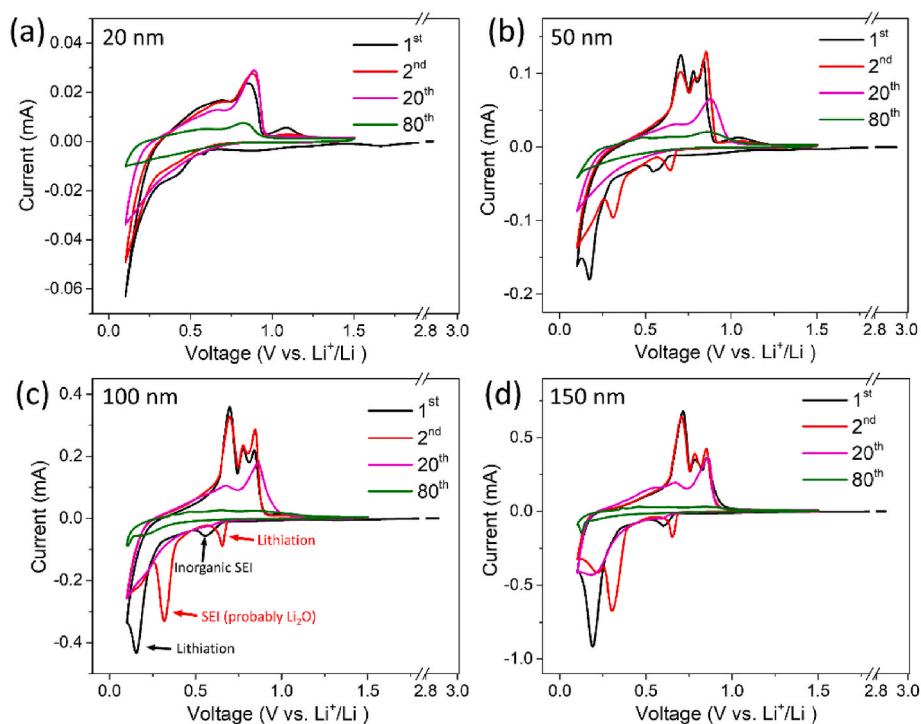


Fig. 3. CV curves of different cycles as labeled for Sn thickness 20 nm (a), 50 nm (b), 100 nm (c) and 150 nm (d) at a scan rate of 0.5 mV/S in a potential window of 0.1–1.5 V.

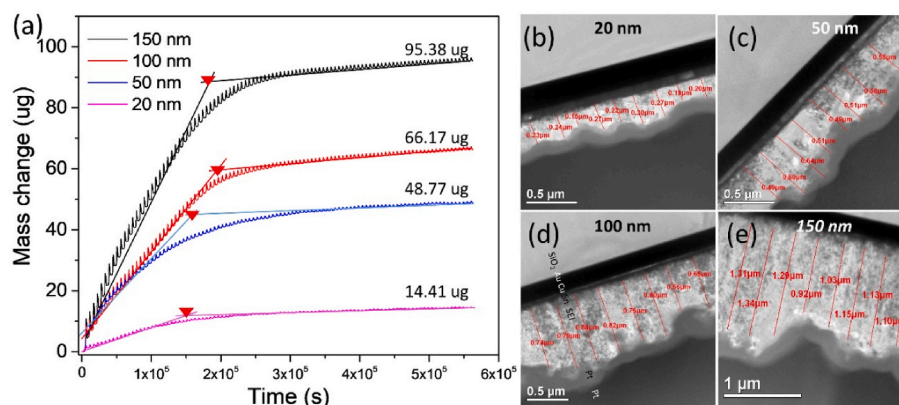


Fig. 4. (a) Mass changes of different sample thicknesses (20 nm, 50 nm, 100 nm, and 150 nm) measured by QCM from the 1st cycle to the 100th cycle. (b–e) TEM micrographs of electrodes of different thickness after 100 cycles (b) 20 nm, (c) 50 nm, (d) 100 nm and (e) 150 nm.

context and strikingly different to similar measurements of Si and  $V_2O_5$  reported earlier [26,27], the SEI mass systematically increases with the Sn thickness, which strongly suggests a significant consumption of Sn by the SEI formation. After 100 cycles, the irreversible mass uptake of the four samples are 14.41  $\mu\text{g}$  (20 nm), 48.77  $\mu\text{g}$  (50 nm), 66.17  $\mu\text{g}$  (100 nm) and 95.38  $\mu\text{g}$  (150 nm) which corresponds to the areal mass loading as shown in Table 1. Moreover, TEM cross section micrographs were investigated to determine the SEI thickness of these four samples after finishing 100 cycles as shown in Fig. 4(b–e). The shown layer structures consist of three major parts: Substrate ( $\text{SiO}_2$ , very thin Ti and Au), the left-over of the electrode (Cu, Sn and SEI) and a protecting layer for lamella lift-out (Pt) (as labeled in Fig. 4 (d)). On course scale, the SEI appears to have fully consumed the initial Sn layer. For a thickness determination of this thick SEI, many positions along the interface were evaluated and averaged to compensate for the roughness. As shown in Table 1, the average TEM thickness of the SEI on 20 nm, 50 nm, 100 nm and 150 nm Sn anodes are  $228 \pm 4.5$  nm,  $546 \pm 5.7$  nm,  $745 \pm 9.0$  nm and  $1158 \pm 13.5$  nm, respectively.

Repeated TEM characterizations of independent samples were performed to reliably estimate error margins. (See examples in Fig. S2 supplementary materials). The thickness of the visible SEI layer in the TEM micrographs may be reasonably understood by a linear relation (solid line (red) in Fig. 5 (a)). Similarly, the mass change per area, measured by QCM after 100 cycles, is also well represented by a linear relation (solid line (red) in Fig. 5 (b)). The corresponding equations are shown in equations (6) and (7), respectively.

$$Y_{SEI} = (7.6 \pm 0.8) X_{Sn} + (78.2 \pm 16.8) \text{ nm} \quad (6)$$

$$M_{SEI} = (1.42 \pm 0.212) X_{Sn} + (24.22 \pm 20.35) \mu\text{g}/\text{cm}^2 \quad (7)$$

where  $Y_{SEI}$ ,  $M_{SEI}$  and  $X_{Sn}$  represent the SEI thickness, SEI mass per area and tin thickness, respectively. The comparison between TEM thickness and SEI mass will be discussed afterwards.

Apart from the thickness or mass uptake at the end of cycling, the uptake of irreversible SEI mass in Fig. 4 (a) is reasonably split into two

parts (the position marked by red triangles may represent the dividing boundary): A first part (including stages I, II and III of SEI formation) indicating constant growth rate (linear growth) which is probably attributed to a mechanism of frequent Sn cracking, while the slow and gradually decreasing growth rate in the subsequent second part (stage IV) might be understood as diffusion controlled (parabolic) growth. In the linear growth, thicker samples produce more SEI per cycle (higher slope of the trendline), which is understandable since the average crack length in thicker samples might be larger than in thin samples. As discussed in previous work [28], after cycling, there is still some pure Sn left inside the electrode. As shown in Fig. 4 (b)–(e), the many black spherical particles (BSP) distributed in the SEI could be shown to be mainly composed of Sn element [28]. Remarkably, as shown in Fig. S4 (a') – (d') in all four electrodes of different thickness, the BSP have similar diameter (20–30 nm), if regions with significant agglomeration are excluded from evaluation. Thus, we strongly believe that with cycling, the Sn films crack until a stable size or thickness of fragments ( $X_0 \approx 30$  nm) is achieved. This moment marks the transition from fast linear to decelerating diffusional growth. So, equation (6) may be better stated as:

$$Y_{SEI} = 7.6 \cdot (X_{Sn} - X_0) + A \quad (8)$$

Where A is a constant thickness offset which equals to  $78.2 \text{ nm} + 7.6 X_0 > 0$ .

As reflected in equation (8), there is indeed a major contribution that is proportional to the Sn thickness and so can be assigned to Sn cracking and the consequent oxidation of the Sn. The thickness-independent contribution A has to be attributed to both the usual SEI formed at the surface in the very first cycle by electrolyte decomposition and the slow diffusional growth which is very similar for all the studied electrode thicknesses.

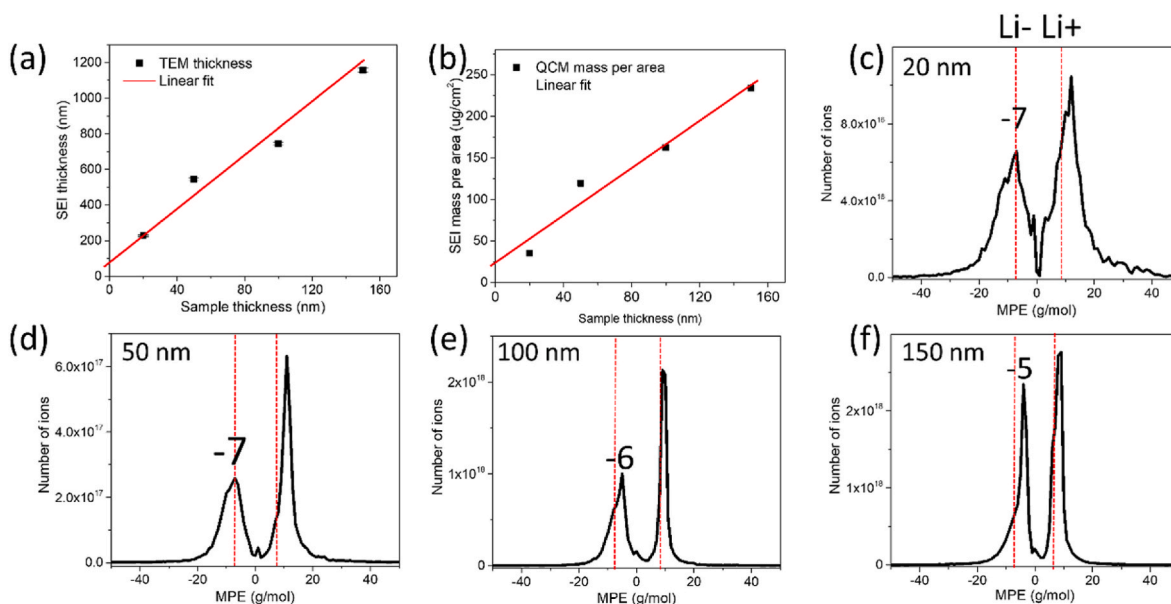
To further confirm the significant contribution of the Sn oxidation to the SEI, the mass spectra averaged on all performed cycles of different electrode thickness are shown in Fig. 5 (c)–(f). As discussed in the previous work at the example of 100 nm thick films [28], the surprising shift of the delithiation peak to absolute values even smaller than 7 can be attributed to the oxidization of Sn, since it compensates part of the mass loss during lithiation, as expressed by Eqs. (9a), (9b). Quantitatively, this peak shift must depend on the relative contribution of Sn oxidization to the overall reaction. Only if no  $\text{SnO}_x$  is forming, the delithiation peak can be exactly centered at  $-7$  g/mol. The observed shift (Eq. (10)) may be quantitatively expressed as in Eqs.(10, 11).  $Q_{Sn}$  is the charge transfer due to oxidization of Sn, which adds half the mass of oxygen per elementary charge, while  $Q_{de}$  represents the total charge transfer measured in the delithiation half cycle.



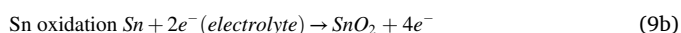
Table 1

The comparison between QCM and TEM results on the SEI thickness and the resulting average density.

Sample	20 nm	50 nm	100 nm	150 nm
QCM Mass ( $\mu\text{g}/\text{cm}^2$ )	35.34	119.57	162.41	233.91
TEM thickness (nm)	$228 \pm 4.5$	$546 \pm 5.7$	$745 \pm 9.0$	$1158 \pm 13.5$
Density of SEI ( $\text{g}/\text{cm}^3$ )	$1.55 \pm 0.06$	$2.19 \pm 0.01$	$2.18 \pm 0.01$	$2.02 \pm 0.03$
Deviations from averaged SEI density of $2.18 \text{ g}/\text{cm}^3$	$-40.7 \pm 2.7\%$	$+0.5 \pm 1.3\%$	$+0.1 \pm 1.2\%$	$-7.9 \pm 1.3\%$



**Fig. 5.** the relationship between initial Sn thickness with SEI thickness after 100 cycles as determined by TEM measurement (a), and SEI mass per area after 100 cycles as measured by QCM (b), the over-all QCM mass spectra of different thickness Sn (c) 20 nm, (d) 50 nm, (e) 100 nm and (f) 150 nm. The exact positions of the delithiation peaks are labeled within the figures.



$$\Delta MPE = \text{Average MPE} - \text{MPE of delithiation} \quad (10)$$

$$\Delta MPE = \left\{ 8 \frac{Q_{\text{Sn}}}{Q_{\text{dc}}} - 7 \left( 1 - \frac{Q_{\text{Sn}}}{Q_{\text{dc}}} \right) \right\} - (-7) = 15 \frac{Q_{\text{Sn}}}{Q_{\text{dc}}} = 15 \frac{\frac{Q_{\text{Sn}}}{\text{volume}}}{\frac{Q_{\text{dc}}}{\text{volume}}} \quad (11)$$

To characterize the SEI in more detail, the QCM mass change can be linked to the TEM thickness to calculate the density of the SEI by using Equation (12) (see Table 1).

$$\bar{\rho} = \frac{\Delta m_{\text{QCM}}}{\text{surface area} \times \text{TEM thickness}} \quad (12)$$

This calculated density can be compared to the commonly reported value of the averaged density i.e. 2.18 g/cm<sup>3</sup> [25,27,28]. As shown in Table 1, with exception of the 20 nm film, the density of the SEI is well in the error range (the standard deviation of the TEM measurement is considered to be ±10%). In the case of the 20 nm film, however, a significant deviation of (40.7 ± 2.7) % is observed between actual density and the generally accepted average density of 2.18 g/cm<sup>3</sup>. To understand this anomaly, we compare the density of different species which could be present in the SEI in Table S1. There is a pronounced difference between the density of the organic and inorganic species. Thus, compared to the thicker films, the SEI on 20 nm Sn may be interpreted as being an organic-rich layer. The MPE-based analysis shown in Figs. S4–S6 of the supplementary materials further supports this

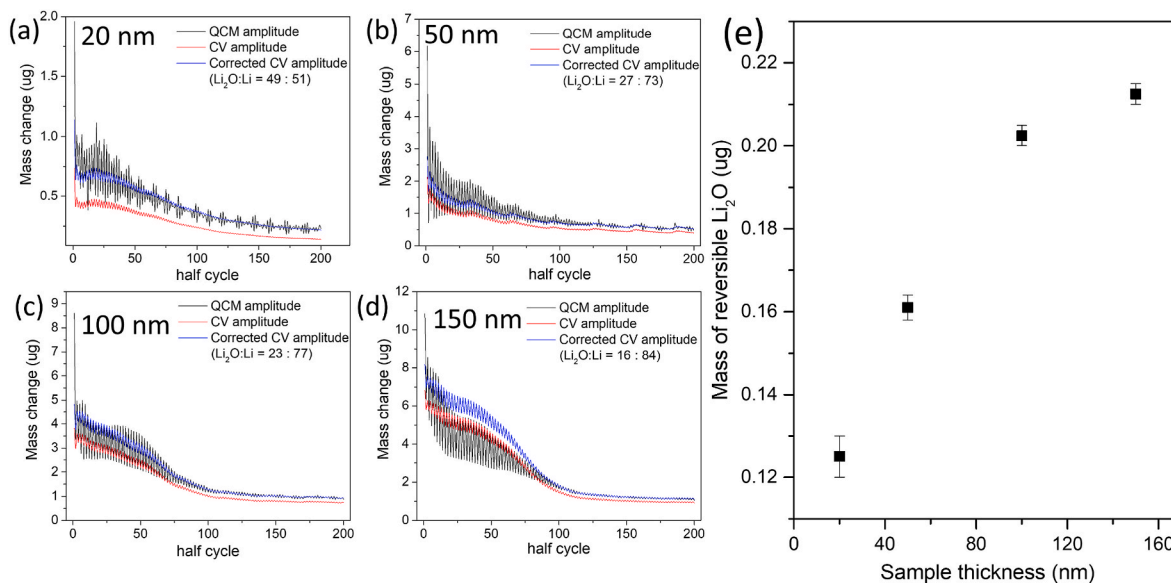


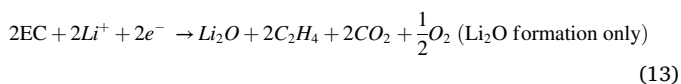
**Fig. 6.** The reversible mass change observed for different Sn thickness (a) 20 nm, (b) 50 nm, (c) 100 nm and (d) 150 nm measured by QCM (black), calculated from CV under assumption of exclusive lithiation (red), derived from CV under assumption of fitted ratio (as labeled) between Li<sub>2</sub>O and Li (blue) and (e) the dependence of the mass of reversible Li<sub>2</sub>O versus the Sn thickness. (For interpretation of the references to colour in this figure legend, the reader is referred to the Web version of this article.)

conclusion.

The second main aspect of the QCM curves are the amplitude of the periodic oscillations. It were strictly calculated by using the ending mass of each half cycle minus its starting mass, while the CV mass oscillations were calculated from the processed charge under the assumption that only Li ions are reversibly processed. As shown in Fig. 6(a–d), the mass oscillations of QCM (black) are systematically larger than those derived from the CV (red). Obviously, there must be at least another heavier species that is reversibly processed. As discussed and evaluated in the previous work [28], the quantitative data reveal the mass of Li<sub>2</sub>O as a second reversibly processed species on Sn anodes. Following a strategy of our previous work [27], the relative contributions of Li<sub>2</sub>O and Li may be adapted to match the CV mass to the QCM data (blue) (exactly we used the data of the 99th and 100th cycle). In this way, the proportion of reversibly processed Li<sub>2</sub>O with respect to the alloyed Li ions is estimated to 49%, 27%, 23% and 16% on 20 nm, 50 nm, 100 nm and 150 nm Sn, respectively. However, since the absolute amount of alloyed Li increases with thickness, the total amount of Li<sub>2</sub>O, nevertheless, increases with Sn thickness. Fig. 6 (e) points out this systematic dependence on the electrode thickness.

It has been argued that (i) the oxygen to produce Li<sub>2</sub>O may stem from the decomposition of the electrolyte [28] and (ii) the formation of Li<sub>2</sub>O must be an interfacial phenomenon. Thus, to first approximation the amount of Li<sub>2</sub>O should be only dependent on the surface area of electrode. But in view of the necessary driving force, it has been suggested that the formation of Li<sub>2</sub>O is controlled by the over-potential required for lithiation [27]. This appears to be corroborated by the experiments presented here. Since a higher overpotential is required to drive the diffusion into thicker films when cycled at the same rate, a larger amount of Li<sub>2</sub>O is produced with increasing Sn thickness.

So far, we have not discussed the possible reaction responsible for the reversible formation of the Li<sub>2</sub>O. In the literature, the formation of Li<sub>2</sub>O on the SEI has been reported to follow Eq. (13):



However, the reversion of this reaction seems to be impossible as the oxygen would escape the system. Similarly, the alternative direct decomposition of the oxide into Li ions and oxygen would need enormous driving force that is not achieved in the studied low voltage range. Thus, desorption of the mass of Li<sub>2</sub>O in the delithiation half cycles, requires a reaction with certain components of the electrolyte that would compensate part of the necessary driving force. At our present knowledge, we cannot identify this reaction although the loss of the specific MPE of 15 amu is clearly demonstrated in the experiments.

### 3.3. The SEI formation under different potential windows of cycling

Both lithiation and SEI formation of Sn are expected to depend on the operation voltage range. Widening at the lower margin towards zero voltage vs Li/Li<sup>+</sup> inserts more lithium. However, attributed to the consequent larger volume expansion, the electrode cracking would be promoted, which exposes more fresh Sn to the electrolyte. Hence, it may result in emphasized SEI formation. By variation of the voltage range, although the role of the irreversible Li<sub>2</sub>O, formed predominantly in the stage II within the voltage window of 0.36–0.27 V, can be further investigated.

First, ex-situ XPS measurements of 100 nm thick films processed in the second cycle to different voltage cut-off were performed to clarify the species formed. The XPS clearly documents that the species formed within 0.36–0.27 V (II stage) are mainly Li<sub>2</sub>O and barely Li<sub>2</sub>CO<sub>3</sub> (see Fig. S7 in supplementary material).

Next, in order to investigate the effects of the potential window of cycling on the electrochemical behavior of Sn anode, 100 nm thick Sn electrodes were cycled in different voltage ranges, namely 0.01–1.5 V,

0.1–1.5 V, 0.2–1.5 V and 0.4–1.5 V. In the following, the results of these experiments will be labeled as Sn0.01, Sn0.1, Sn0.2 and Sn0.4, respectively. Fig. 7 (a) shows the CV curve of Sn0.01. After longer cycling, abnormal peaks appeared (see blue curve in Fig. 7 (a)). Considering the potential as low as 0.01 V, these peaks are probably derived from reactions after the electrode cracking. A TEM cross-section image and the corresponding EDX map are shown in Fig. 7 (b) and Fig. 7 (c), respectively. It becomes clear that the Sn anode, the current collector (Cu) and even part of the substrate (Au) have cracked as has been also independently reported elsewhere [30]. Due to the overlapping mass changes in Sn, Cu and Au, it is almost impossible to study the electrode material independently. Hence, we did not further analyze this sample.

To demonstrate the role of inorganic SEI formed in stage II in the voltage range of 0.36–0.27 V, CV measurements with different lower boundary of the voltage window were performed as shown in Fig. 7 (d–f). Cycled down to 0.1 and 0.2 V, as in Fig. 7 (d) and (e), the CV curves show a redox performance that closely resembles the already discussed behavior. In consequence, also the QCM mass changes (black and blue in Fig. 7 (g)) are very close, both reaching the stage of very slow parabolic SEI growth. However, when the formation of the inorganic SEI in the voltage range of 0.27-to 0.36V is suppressed by elevating the lower cycling boundary to 0.4 V, the irreversible mass uptake continuous the initial stage of linear growth (Fig. 7 (g), red), and in consequence, the final SEI mass (77.8 μg) becomes considerably bigger.

It is generally accepted that the SEI can chemically insulate the electrode from the electrolyte to prevent further decomposition of the latter. On the contrary, here, the SEI seems to be continuously forming when cycled only down to 0.4 V. Thus, the surfaces of the three samples were checked by SEM for their microstructure. As shown in Fig. 8 (a), and (b), the surfaces of Sn0.1 and Sn0.2 are rather smooth and dense, but Sn0.4 shows an uneven and porous morphology, which cannot effectively protect the electrolyte from decomposition, anymore. Thus, we can conclude that the irreversibly Li<sub>2</sub>O that predominantly forms in the voltage range 0.36–0.27 V controls the microstructure and properties of the SEI decisively.

In addition, XRD was conducted to study the crystal structure of the electrode after cycling, as shown in Fig. 8 (d). For as-deposited Sn, the peaks at 43.8° and 44.9° correspond to Sn (220) and (221), respectively, while the peak at 43.2° is a signal of the additional current collector (Cu). Remarkably, the XRD spectra of Sn0.1, Sn0.2 and Sn0.4 do not show any significant difference. In agreement with previous work [28], disappearance of the Sn reflection and appearance of a new peak at 26.6° after cycling just represents the reaction of Sn to SnO<sub>2</sub> (100) or Li<sub>2</sub>SnO<sub>3</sub> (112). Thus, obviously the reason for the different microstructure when cycled only down to 0.4 V must be attributed to amorphous structures or material which otherwise escapes the sensitivity of XRD and so supports the important role of the amorphous or nano-grained SEI.

To search for even delicate chemical variations, various XPS of surface and volume were taken as shown in Fig. 8. The Li peak is shown in the first column, Fig. S9 (a)–(d), the oxygen in the second, Fig. S9 (a') - (d'), and the tin peak in the third row, Fig. S9 (a'') - (d''). The surface and volume of SEI formed on Sn0.1 and Sn0.4 all show a Li–Li signal (around 54.6 eV) caused by incomplete delithiation. However, the indication of Li<sub>2</sub>O is only seen in Fig. S9 (c) (Li1s–Li<sub>2</sub>O) and (c') (O1s–Li<sub>2</sub>O) in the volume of Sn0.1. Obviously, cycling to low voltage boundary is required to form the Li<sub>2</sub>O. The necessary potential window to form the oxide has been further demonstrated (see Fig. S7 supplementary material). Besides, as shown in Fig. S9 (b') and (d''), the signal part of the O 1s peak at 528.8 eV assigned to organic species (RO–Li, blue) is observed on the surface and inside the volume of Sn0.4, which demonstrates that without Li<sub>2</sub>O, the SEI cannot prevent the decomposition of electrolyte and consequent significant formation of organic species. The Sn oxidation is finally reflected by the Sn 3d spectra as shown in Fig. S9 (a'') - (d''). There is no signal of pure Sn on both surfaces but significant portion of pure Sn remains in the volume after 100 cycles of Sn0.1 and

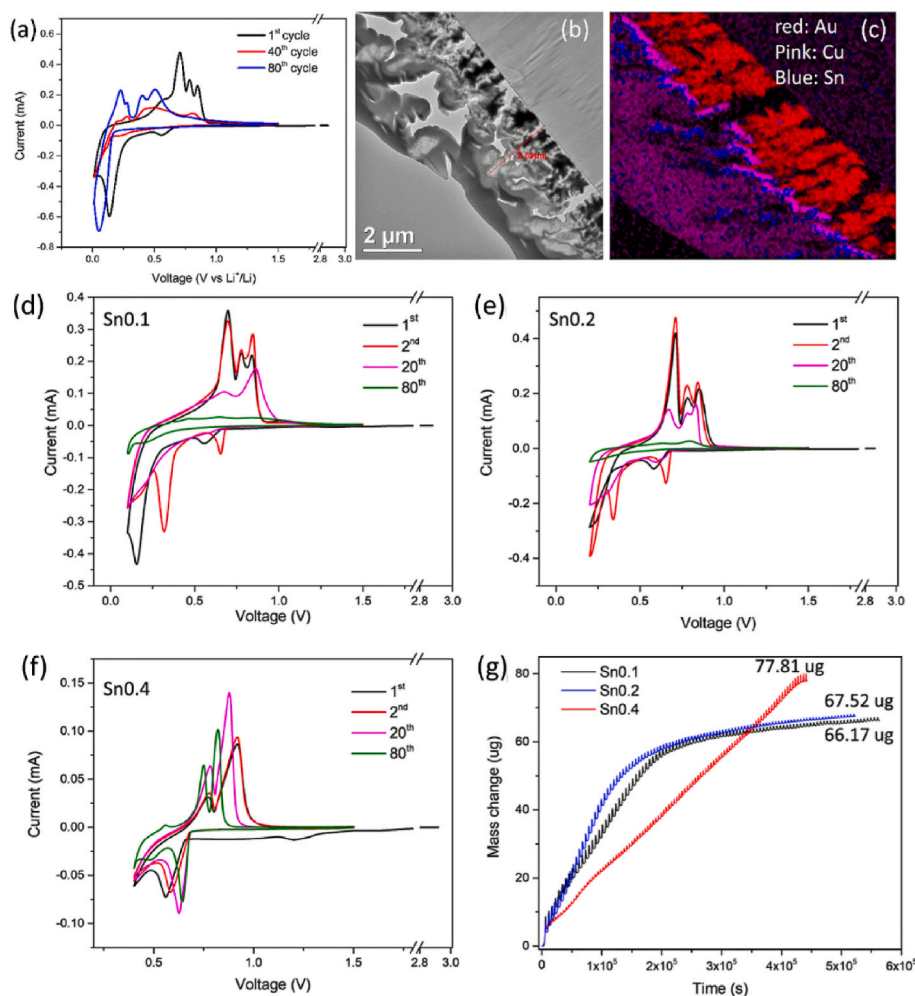


**Fig. 7.** (a) CV curves of a 100 nm Sn electrode at a scan rate of 0.5 mV/s in a potential window of 0.01–1.5 V. (b) TEM micrograph of Sn0.01 after cycling, (c) the corresponding EDX mapping of the TEM micrograph (Au (red), Cu (pink) and Sn (blue)). CV curves of a 100 nm Sn electrode cycled at 0.5 mV/s in a potential window of (d) 0.1–1.5 V, (e) 0.2–1.5 V, (f) 0.4–1.5 V and (g) corresponding QCM mass changes (0.1–1.5 V, 0.2–1.5 V and 0.4–1.5 V). (For interpretation of the references to colour in this figure legend, the reader is referred to the Web version of this article.)

Sn0.4, as well. Although, the porous predominantly organic SEI in the case of Sn0.4 cannot well protect the electrode, the smaller volume expansion and thus less cracking due to only shallow lithiation, may prevent Sn from fully transforming into Sn oxide.

#### 4. Conclusion

Quartz crystal microbalance (QCM) and Cyclic Voltammetry (CV) were combined to investigate the impact of Sn thickness and potential window on the SEI formation during battery cycling of a Sn anode. Mass change per charge was calculated by combining the results of CV (change of charge) and QCM (change of mass), which allows to distinguish different stages of SEI formation. Results were further corroborated by XPS and XRD data. In addition, the microstructure of SEI was investigated by SEM and TEM, which provides a systematic understanding of SEI formation with Sn electrodes.

It was found that:

1. There is a linear relation between electrode thickness and SEI thickness probably attributed to the intensive Sn cracking and major oxidation of the Sn. Moreover, a critical fragment size ( $X_c$ ) is determined at 20–30 nm. If thickness or remaining fragments  $X_{Sn} > X_c$ , SEI formation is dominated by cracking, else it continues by slow diffusional parabolic growth.
2. The calculation of SEI density via combining the results of QCM and TEM is an efficient method to indicate the composition of SEI. Very thin electrode films promote the organic fraction of the SEI.

3. Besides being a viable part of the SEI, Li<sub>2</sub>O also contributes to reversible charge storage. This study has demonstrated that the relative amount of reversible Li<sub>2</sub>O is correlated with the sample thickness. Specifically, the amount of reversible Li<sub>2</sub>O increases with the electrode thickness, which is probably controlled by the larger over-potential required for lithiation of thicker films.
4. The formation of the inorganic part of the SEI is a thickness- and potential-dependent process. The inorganic SEI consisting of Li<sub>2</sub>O and Li<sub>2</sub>CO<sub>3</sub> plays the most important role in stabilizing the electrode against further corrosion. Without it, the electrolyte continuously decomposes with the consequence of continued linear SEI growth. At the end, the electrode is fully transformed into a porous layer.

#### CRediT authorship contribution statement

**Ke Wang:** has done the experiments and the data analysis while additionally drafting the manuscript. **Yug Joshi:** works with the correction of manuscript. **Hong Chen:** has contributed to the XRD measurement. **Guido Schmitz:** is the supervision of the experiments and correction of the manuscript.

#### Declaration of competing interest

The authors declare that they have no known competing financial interests or personal relationships that could have appeared to influence the work reported in this paper.



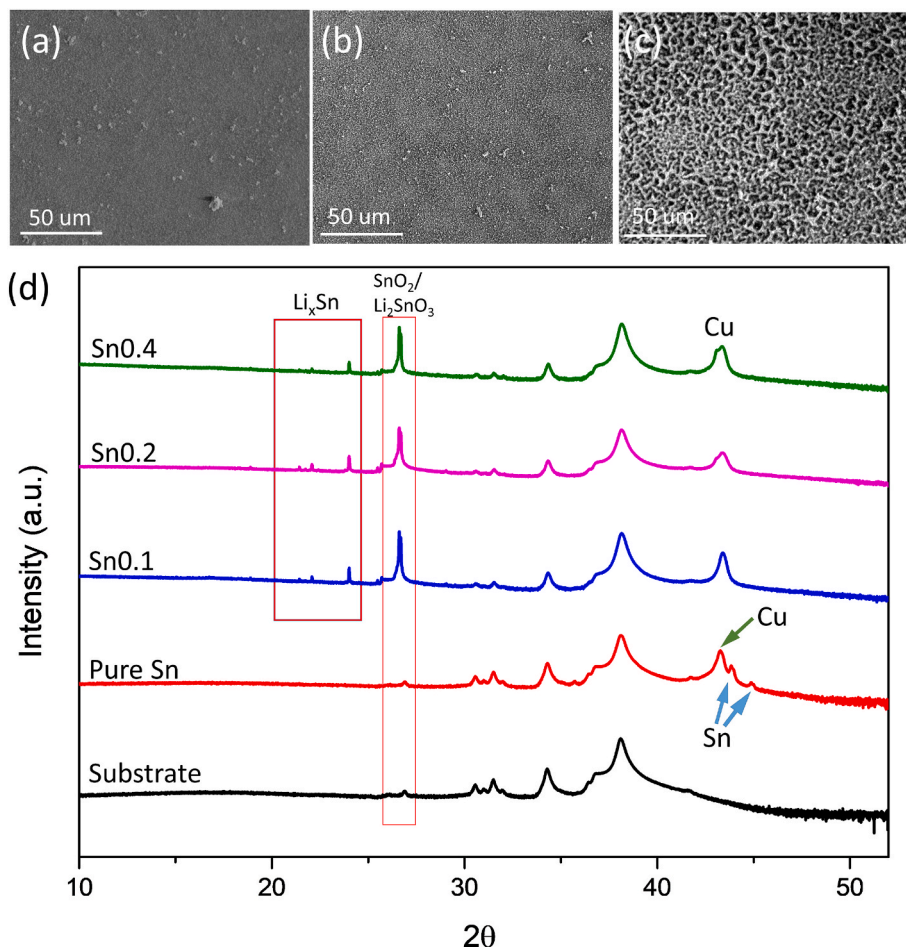


Fig. 8. SEM images of (a) SnO.1, (b) SnO.2, (c) SnO.4 and (d) XRD pattern of substrate, bare Sn and electrodes after respectively cycling down to 0.1 V, 0.2 V or 0.4 V.

#### Data availability

The data that has been used is confidential.

#### Acknowledgements

This work was funded by the Deutsche Forschungsgemeinschaft (DFG, German Research Foundation) –Project number 492318587 (SCHM 1182/25–1). We are also very grateful to the China Scholarship Council (CSC, China) that supported the PHD work of Ke Wang. YJ is grateful to BMBF for the funding of the Project Aqua IQ-EL.

#### Appendix A. Supplementary data

Supplementary data to this article can be found online at <https://doi.org/10.1016/j.jpowsour.2023.232919>.

#### References

- [1] J.B. Goodenough, Y. Kim, Challenges for rechargeable Li batteries, *Chem. Mater.* 22 (2010) 587–603.
- [2] F. Wu, J. Maier, Y. Yu, Guidelines and trends for next-generation rechargeable lithium and lithium-ion batteries, *Chem. Soc. Rev.* 49 (2020) 1569–1614.
- [3] X. Fan, C. Wang, High-voltage liquid electrolytes for Li batteries: progress and perspectives, *Chem. Soc. Rev.* 101 (2021).
- [4] A.R. Kamali, D.J. Fray, Tin-based materials as advanced anode materials for lithium ion batteries: a review, *Rev. Adv. Mater. Sci.* 27 (2011) 14–24.
- [5] L. Liu, et al., Tin-based anode materials with well-designed architectures for next-generation lithium-ion batteries, *J. Power Sources* 321 (2016) 11–35.
- [6] A. Gajan, et al., Solid electrolyte interphase instability in operating lithium-ion batteries unraveled by enhanced-Raman spectroscopy, *ACS Energy Lett.* 6 (2021) 1757–1763.
- [7] K.S. Eom, et al., Improved stability of nano-Sn electrode with high-quality nano-SEI formation for lithium ion battery, *Nano Energy* 12 (2015) 314–321.
- [8] E. Peled, S. Menkin, Review—SEI: past, present and future, *J. Electrochem. Soc.* 164 (2017) A1703–A1719.
- [9] W. Liu, P. Liu, D. Mitlin, Review of emerging concepts in SEI analysis and artificial SEI membranes for lithium, sodium, and potassium metal battery anodes, *Adv. Energy Mater.* 10 (2020) 1–24.
- [10] S.K. Heiskanen, J. Kim, B.L. Lucht, Generation and evolution of the solid electrolyte interphase of lithium-ion batteries, *Joule* 3 (2019) 2322–2333.
- [11] Y. Li, et al., How can the electrode influence the formation of the solid electrolyte interface? *ACS Energy Lett.* 6 (2021) 3307–3320.
- [12] A. Wang, S. Kadam, H. Li, S. Shi, Y. Qi, Review on modeling of the anode solid electrolyte interphase (SEI) for lithium-ion batteries, *npj Comput. Mater.* 4 (2018).
- [13] L.Y. Beaulieu, T.D. Hatchard, A. Bonakdarpour, M.D. Fleischauer, J.R. Dahn, Reaction of Li with alloy thin films studied by in situ AFM, *J. Electrochem. Soc.* 150 (2003) A1457.
- [14] M. Sina, et al., Direct visualization of the solid electrolyte interphase and its effects on silicon electrochemical performance, *Adv. Mater. Interfac.* 3 (2016) 1–10.
- [15] X. Chen, M. Shang, Niu, J. Pre-solid electrolyte interphase-covered Li metal anode with improved electro-chemo-mechanical reliability in high-energy-density batteries, *ACS Appl. Mater. Interfaces* 13 (2021) 34064–34073.
- [16] Y. Gao, et al., General method of manipulating formation, composition, and morphology of solid-electrolyte interphases for stable Li-alloy anodes, *J. Am. Chem. Soc.* 139 (2017) 17359–17367.
- [17] C.S. Nimisha, G. Venkatesh, K.Y. Rao, G.M. Rao, N. Munichandraiah, Morphology dependent electrochemical performance of sputter deposited Sn thin films, *Mater. Res. Bull.* 47 (2012) 1950–1953.
- [18] R. Hu, et al., Dramatically enhanced reversibility of Li<sub>2</sub>O in SnO<sub>2</sub>-based electrodes: the effect of nanostructure on high initial reversible capacity, *Energy Environ. Sci.* 9 (2016) 595–603.
- [19] K.W. Noh, S.J. Dillon, Morphological changes in and around Sn electrodes during Li ion cycling characterized by in situ environmental TEM, *Scripta Mater.* 69 (2013) 658–661.
- [20] N. Shpigiel, et al., In situ monitoring of gravimetric and viscoelastic changes in 2D intercalation electrodes, *ACS Energy Lett.* 2 (2017) 1407–1415.
- [21] V. Dargel, et al., In situ real-time gravimetric and viscoelastic probing of surface films formation on lithium batteries electrodes, *Nat. Commun.* 8 (2017).

- [22] N. Shpigel, M.D. Levi, S. Sigalov, L. Daikhin, D. Aurbach, In situ real-time mechanical and morphological characterization of electrodes for electrochemical energy storage and conversion by electrochemical quartz crystal microbalance with dissipation monitoring, *Acc. Chem. Res.* 51 (2018) 69–79.
- [23] G. Sauerbrey, Verwendung von Schwingquarzen zur Wägung dünner Schichten und zur Mikrowägung, *Z. Phys.* 155 (1959) 206–222.
- [24] T. Liu, et al., In situ quantification of interphasial chemistry in Li-ion battery, *Nat. Nanotechnol.* 14 (2019) 50–56.
- [25] Z. Yang, M.C. Dixon, R.A. Erck, L. Trahey, Quantification of the mass and viscoelasticity of interfacial films on tin anodes using EQCM-D, *ACS Appl. Mater. Interfaces* 7 (2015) 26585–26594.
- [26] J. Terwort, F. Berkemeier, G. Schmitz, Li<sub>x</sub>V<sub>2</sub>O<sub>5</sub> – analysis of surface reactions by spectroscopic quartz crystal microgravimetry, *J. Power Sources* 336 (2016) 172–178.
- [27] T. Kohler, E. Hadjixenophontos, Y. Joshi, K. Wang, G. Schmitz, Reversible oxide formation during cycling of Si anodes, *Nano Energy* 84 (2021), 105886.
- [28] K. Wang, Y. Joshi, H. Chen, G. Schmitz, In-situ analysis of solid-electrolyte interphase formation and cycle behavior of Sn battery anodes, *J. Power Sources* 535 (2022), 231439.
- [29] Q. Li, et al., Study of copper foam-supported Sn thin film as a high-capacity anode for lithium-ion batteries, *Electrochim. Acta* 54 (2009) 5884–5888.
- [30] P. Bach, M. Stratmann, I. Valencia-Jaime, A.H. Romero, F.U. Renner, Lithiation and delithiation mechanisms of gold thin film model anodes for lithium ion batteries: electrochemical characterization, *Electrochim. Acta* 164 (2015) 81–89.